Materials Advances

ROYAL SOCIETY OF CHEMISTRY

PAPER

View Article Online
View Journal | View Issue

Cite this: *Mater. Adv.*, 2023, 4, 6367

The synthesis and combined electrical–magnetic and toxic dye sequestration properties of a Cr(III)-metallogel†

Krishna Sundar Das,[a] Mainak Das,[b] Sayan Saha,[a] Amit Adhikary,[a] Sukhen Bala,[a] Partha Pratim Ray*[b] and Raju Mondal*[a]

Materials based on typical inorganic compounds, along with their embodied metal-specific features like redox, magnetic, catalytic and spectroscopic properties, in their as-synthesized economical, end-user friendly and commercially viable gel states, have manifold practical and strategic advantages. Along these lines, the work presented herein aims to explore the usefulness of porous gel-based inorganic compounds, in their original as-synthesized states, for probing their combined electrical, magnetic and adsorption properties. Accordingly, we have synthesized and thoroughly characterized a benzene dicarboxylic acid based Cr(III)-metallogel for magnetic and electrical device fabrication. The metallogel shows an interesting NMOP morphology and is thoroughly characterized using various microscopic and spectroscopic techniques. Furthermore, rheological studies on the resultant metallogel reveal its interesting thixotropic behaviour. The Cr-gel has been successfully utilized for fabricating an electrical Schottky barrier diode with a befitting conductivity value of 1.61×10^{-2} S cm^{-1}. Moreover, the free immobilized azide group, featuring in-built charge-separated resonance structures, acts as a proton carrier facilitator-cum-transporter and shows an impressive proton conductivity value of 3.3×10^{-4} S cm^{-1} at 95% relative humidity and 85 °C. The presence of paramagnetic chromium ions also renders a special physicochemical property, namely magnetism, to the system. The porous and magnetic nature of the as-synthesized metallogel was also evaluated. DC magnetic susceptibility data confirm the antiferromagnetic nature of the material. Gas sorption studies, on the other hand, confirm the porous nature and show the selective CO_2 uptake ability of the xerogel. Subsequently, the as-synthesized, by default porous, magnetic metallogel was utilized as an adsorbent for removing toxic organic dyes like methylene blue, rhodamine B and crystal violet. Interestingly, the as-prepared metallogel also enables the substantial release of the adsorbed dye molecules for re-use. To the best of our knowledge, this kind of electrical–magnetic Cr-gel based wastewater treatment technique was not reported hitherto in the literature but has a huge potential application in adsorbent based environmental remediation as well as in magnetic or electrical device fabrication.

Received 1st September 2023,
Accepted 30th October 2023

DOI: 10.1039/d3ma00645j

rsc.li/materials-advances

Introduction

Metallogels, comprising typical inorganic metal–ligand coordination bonds, have emerged as some of the front runners in the field of new-age inorganic materials.[1–4] A crucial hurdle that thwarts the metallogels from being the predominant materials is the step that involves arresting a relatively heavy metal-coordinated network in its less-ordered gel state while using nothing more than a common low-molecular-weight ligand for gelation.[5–7] The consequential low-success rates play a major role in deterring inorganic chemists from conducting metallogelation studies. Two other contributing factors of this apathy would be: (a) for inorganic compounds, metallogelation mostly happens serendipitously rather than by design and (b) low structural predictability, which is deduced from guessing various possible self-assembly methods.[8,9] The gel state, by default, represents the short range ordering of gelators and solvent molecules in nanoscale dimensions. Naturally, the studies of their self-assembly also demand nano-level instrumentation and nanostructural techniques such as scanning electron microscopy (SEM), transmission electron microscopy (TEM), atomic force microscopy (AFM) and X-ray photoelectron

[a] School of Chemical Sciences, Indian Association for the Cultivation of Science, Raja S. C. Mullick Road, Kolkata 700032, India. E-mail: icrm@iacs.res.in
[b] Department of Physics, Jadavpur University, Raja S. C. Mullick Road, Jadavpur, Kolkata 700 032, India

† Electronic supplementary information (ESI) available. See DOI: https://doi.org/10.1039/d3ma00645j

spectroscopy (XPS). In other words, studies on the self-assembled nanostructures are more concerned about the shapes, sizes, morphologies or surface phenomena of the bulk materials, which are markedly different from those of the conventional molecular-level self-assembled inorganic compounds.[10–12] Notwithstanding, generating inorganic compounds, along with their embodied metal-specific properties including redox, magnetic, catalytic and spectroscopic properties, in their economical, as-synthesized, often much more end-user friendly and commercially viable gel states has manifold practical and strategic advantages.[13–15]

Interestingly, a special branch of metallogels that are formed by encapsulating a large amount of solvent molecules inside their highly cross-linked, intertwined coordination polymeric networks can be envisaged as the short-range ordered aggregated version of crystalline metal–organic frameworks (MOFs) or coordination polymers.[16–18] The MOFs have emerged as the most important class of multifunctional materials with a wide range of applications including magnetic and electrical device fabrication, adsorption, separation, and environmental remediation.[19–21] The structural similarity, albeit in a short range, between the coordination polymer based metallogels and crystalline MOFs brings an interesting possibility of replicating the surface features and physicochemical properties in the gel state.[22,23] Of particular interest are the adsorption related applications of the by default porous networks of metallogels along with their magnetic and electrical properties.[24–26] The electrical properties of MOFs depend heavily on the presence of infinite hydrogen bonded networks, which can result from encapsulated solvents or functional groups present inside their frameworks.[27,28] The metallogels that incorporate sufficiently large amounts of solvent molecules and that are sustained by infinite hydrogen bonded networks are therefore a natural choice for the study of their electrical properties.[29,30] Furthermore, the changeover from an ordinary organic ligand to a gelator is usually brought about by various functional groups capable of forming extensive supramolecular interactions including hydrogen bonding interactions.[31,32] Coincidentally, the presence of such immobilized functional groups, strategically grafted inside the polymeric networks, can also facilitate charged species generation and/or transportation, which are considered to be the most essential features required for conductivity-based electrical device fabrication.[33,34] Naturally, various ligands with specific immobilized functionalities like acidic –COOH and $-SO_3H$ or N-heterocyclic rings such as pyrazoles, triazoles, imidazoles, and histamine have been explored in recent years.[35–37]

A notable functionality that is absent from these sets of functionalities would be the azide ($-N_3$) group, despite its well-known resonance structures comprising distinctly charge-separated canonical forms.[38] The azide group, because of its unique covalent bond connectivity, therefore has a natural tendency to instigate charged species generation, which in turn can create a suitable environment to install proton carriers (*e.g.*, H_2O) inside the pores and facilitate proton exchange easily.[39]

Inspired by the aforesaid facts, we choose 5-azidoisophthalic acid (N_3IPA) to evaluate the role of the azide group. The noncoordinating nature of the azide group and the well-known coordination behaviour of carboxylate groups with respect to the hard trivalent chromium centre led us to believe that N_3IPA would be an ideal candidate for our investigation. The reaction of N_3IPA with trivalent chromium (Cr(III)) led to gel formation, which was rather unexpected considering the fact that the dicarboxylate molecule is devoid of any hydrogen bonding group. It is noteworthy here that the encapsulation of a large amount of solvent molecules inside a cross-linked metal–organic network is the essence of metallogel formation.[40,41] The said solvent encapsulation is usually orchestrated by the hydrogen bonds and weak intermolecular interactions between the solvents and ligand molecules fitted with hydrogen bonding functional groups (commonly amide or urea groups). With the azide group as the only non-coordinating functional group, the metallogel formation capability of N_3IPA is therefore quite remarkable. The possible supramolecular interactions between the azide group and solvent molecules are comparatively weak but sufficient enough to arrest a metal-coordinated network in the gel state.

The incorporation of Cr(III) as a magnetic moment carrier enhances the possibility of generating a porous magnetic gel. As such, the magnetic properties of the metallogel were also studied in detail. We were extremely successful in our aim of using the as-prepared magnetic metallogel as an adsorbent material, which was further corroborated by its selective CO_2 gas uptake. The adsorption and release of three representative organic dyes, methylene blue (MB), rhodamine B (RhB), and crystal violet (CV), have also been thoroughly investigated. The electrical properties of the metallogel are consistent with the theme of this work and fully justify the usefulness of the azide group in Schottky barrier diode fabrication with befitting improved photosensitized optoelectronic data. Moreover, detailed variable temperature and humidity dependent proton conductivity data further pinpoint the significance of the metallogel in generating electrical devices.

Result and discussion

Synthesis

The ligand, N_3-IPA, was prepared in its highly crystalline form, following our earlier reported method.[42] Nonetheless, the gel-forming ability of the ligand was explored in a wide range of solvents with varying polarity under various experimental conditions including temperature variation and sonication. The N_3-IPA ligand did not form a gel under the above conditions, even in different pH ranges. The N_3-IPA molecule, however, forms a sufficiently strong metallogel in the presence of Cr(III) nitrate under heating conditions in a DMF/MeOH (1 : 1) solvent system. Although, the metallogelation of N_3-IPA was not specific to the nitrate salt of chromium, as chloride and acetate salts also form gels, the nitrate salt formed the strongest gel. Furthermore, the presence of DMF in the solvent system appeared to be a determining factor in metallogel formation since other polar solvents except DMF led to precipitation.

In order to have an insight into the nature as well as the properties of the metallogel, detailed microscopic and

spectroscopic experiments were performed. Fourier transform infrared (FTIR) spectroscopy was utilized to differentiate the behaviour of the functional groups in their free crystalline and xerogel forms (Fig. S1, ESI†). The carboxylic acid C=O stretching band at 1718 cm^{-1} in the free ligand presents a hump at 1710 cm^{-1} due to metal-coordination. The appearance of new bands in the range of 669–513 cm^{-1} in the IR spectra of the complex can be attributed to Cr–O stretching, confirming metal–ligand coordination. Apart from this, a sharp characteristic peak at 2115 cm^{-1} is observed for the free $-N_3$ group in the xerogel. A slight decrease in $-N_3$ stretching (2121 cm^{-1} for the free ligand) indicates a weak interaction of the $-N_3$ group with the solvent molecules. Furthermore, a characteristic peak for the NO_3^- ions of the metal salt appeared at 1384 cm^{-1} for the xerogel.

The UV-visible spectrum (Fig. S2, ESI†) of the free ligand shows a broad absorption band at about 261 nm, suggesting intraligand π–π* transition. For the gel form, the corresponding absorption maximum remains the same, probably due to no significant aggregation of the polymeric network. Furthermore, an ILCT band which appeared at about 295 nm for the free ligand shifted to a higher absorption region (318 nm) in the gel state due to the formation of a metal–ligand coordination complex.

Subsequently, the Tauc formula was utilized to calculate the optical band gap:[43]

$$\alpha h\nu = A(h\nu - E_g)^n \quad (1)$$

where 'α' is the absorption coefficient, 'E_g' is the band gap, 'h' is Planck's constant, 'ν' is the frequency of light, the exponent 'n' is the electron transition process dependent constant with a value considered to be 1/2, and 'A' is a constant that is considered to be 1 in an ideal case. Accordingly, the E_g of the gel was determined using the above equation by extrapolating the linear region of the plot $(\alpha h\nu)^2$ *vs.* $h\nu$ to $\alpha = 0$ absorption. The calculated E_g value turns out to be 3.44 eV, which indicates that our gel material can be considered as a wide band gap semiconductor (Fig. S2, ESI†).

It is noteworthy that the physicochemical properties including the absorbance and magnetism of metallogels are often found to be linked with the morphology of the system. Accordingly, the morphology of the gel system was studied in detail using various microscopic techniques like transmission electron microscopy (TEM) and field-emission scanning electron microscopy (FESEM) techniques. Both microscopic techniques used on a freshly prepared xerogel reveal a similar morphology, an aggregation of numerous spherical nanoscale metal–organic particles (NMOPs).[44,45] As illustrated in Fig. 1, the diameters of the NMOPs range from 10 nm to 50 nm. Furthermore, energy-dispersive X-ray spectroscopy (EDAX) data confirm the presence of the elements of both the metal and the organic molecule (C, N, O, and Cr) used for gelation (Fig. S3, ESI†). This confirms that the particles produced are indeed NMOPs, made of both metal and organic parts, and also confirms the absence of metallic chromium or chromium oxide nanoparticles. Furthermore, selected-area electron diffraction (SAED) performed on these NMOPs revealed the amorphous nature of the gel.

In order to confirm the gel nature of the compound, the viscoelastic properties were determined using amplitude and frequency sweep experiments performed at a constant temperature of 298 K. The amplitude sweep experiment was performed at a constant 10 rad s^{-1} Angular frequency (w) within a range of 0.01% to 100% shear strain. The crossover of G' and G'' takes place at 24.7% shear strain (Fig. 2(a)) or 210 Pa shear stress (Fig. S4, ESI†). Before the crossover point a linear viscoelastic region (LVE) is observed and the functions of G' and G'' show constant plateau values within the LVE region. The frequency sweep experiment (Fig. 2(b)) was carried out below the critical shear strain within a range of 100 rad s^{-1} to 0.1 rad s^{-1} angular frequency to investigate the viscoelastic nature of the gel and to determine the frequency dependence of storage (G') and loss (G'') moduli. There was no entanglement effect in this range and the storage and loss moduli ran in parallel, which confirm the perfect gel nature.

Interestingly, the metallogel is thixotropic.[46] In other words, the metallogel undergoes a repetitive reversible conversion from the gel to sol state upon the application of certain external stimuli such as mechanical shaking, agitation, *etc*. and returns to the gel state upon removing the external stimuli and resting. The thixotropic nature of the metallogel was proved by performing a typical five-step time sweep experiment. As part of this

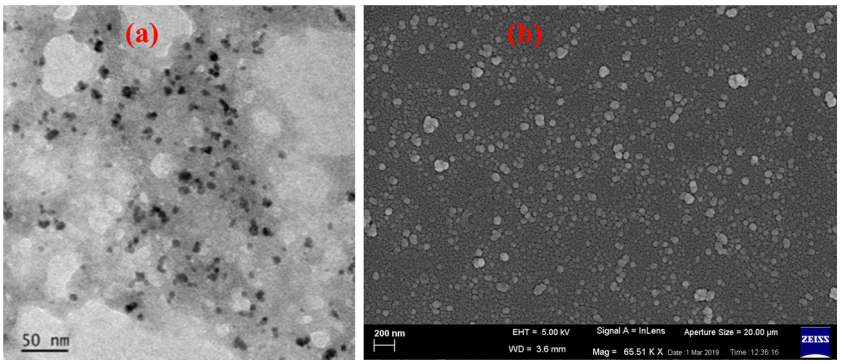

Fig. 1 Selective (a) TEM and (b) SEM images of the metallogel showing the formation of NMOPs.

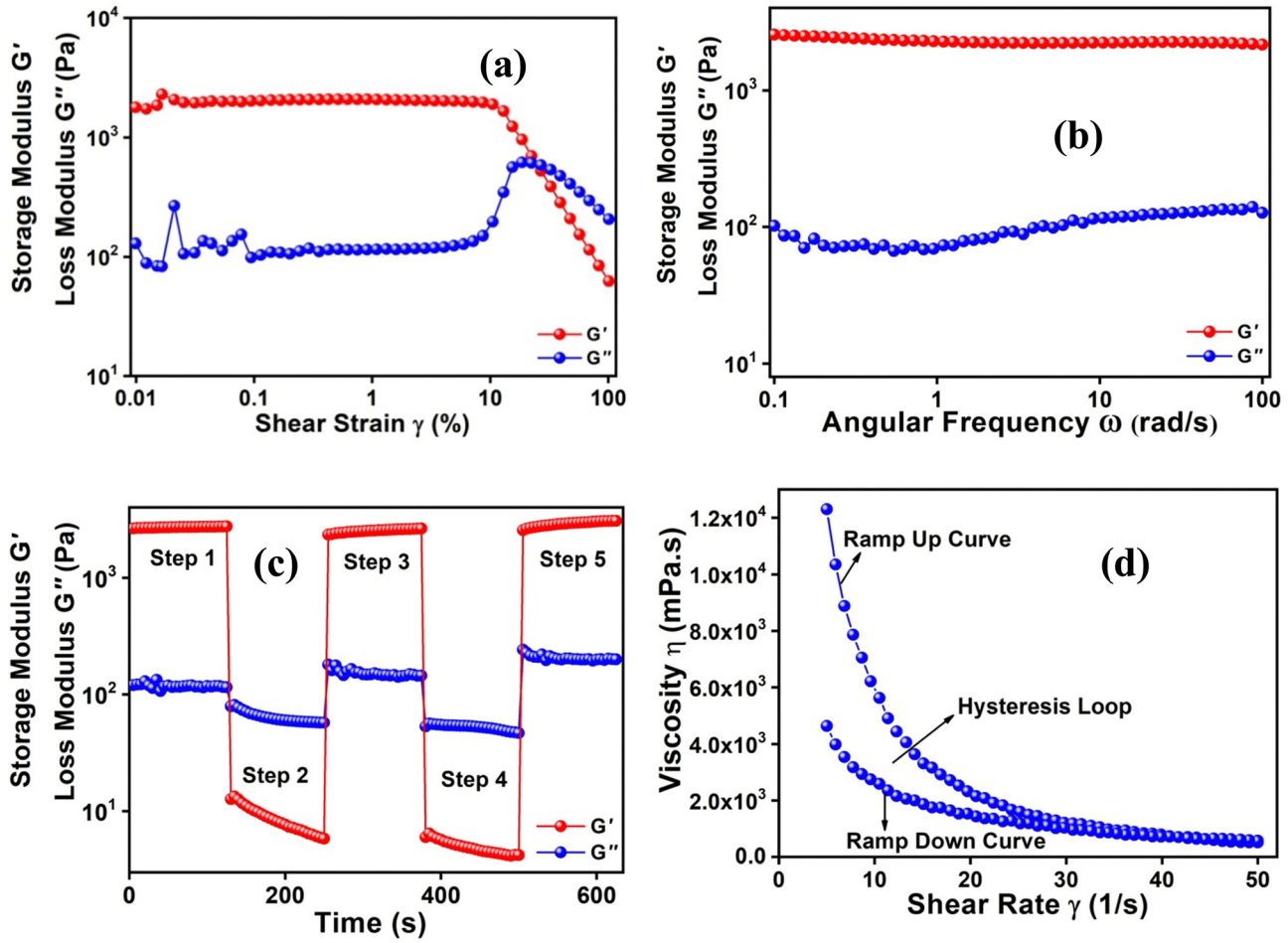

Fig. 2 Rheological data of the gel showing (a) the strain sweep test of the gel, (b) the frequency sweep of the gel, (c) the time sweep experiment to prove its thixotropic nature and (d) the corresponding hysteresis loop test.

experiment, (Fig. 2(c)) the sample was sequentially subjected to low (0.5%) and high strains (100%), separated by a certain amount of time to ensure complete conversion. The application of low strain sustains the gel-state ($G' > G''$), whereas the application of higher strain ruptures the gel state and leads to gel-to-sol ($G'' > G'$) conversion, resulting in the sol state, which upon the application of low strain reverts back to the gel state. The thixotropic behaviour was further crosschecked *via* hysteresis loop formation (Fig. 2(d)).[47] As part of the three-step loop test, the viscosity of the gel was measured by varying the shear rates (a) in the range of 5 s^{-1} to 50 s^{-1} (b) at a fixed 50 s^{-1} and (c) in the range of 50 s^{-1} to 5 s^{-1}. It is imperative note here that the appearance of the thixotropic behaviour of N_3IPA as a gelator is really intriguing, considering its limited scope of forming supramolecular interactions, which is the most essential perquisite to bring about the necessary structural reorganization at the microscopic level.

Metallogel for electrical device fabrication

As for the current contribution, the Cr-based metallogel was used for Schottky barrier diode (SBD) fabrication and proton conductivity measurements. This propelled us to utilize our material for diode fabrication using an ITO/Cr-gel/Al sandwich thin film. The device has been developed following the method reported in our earlier work[48] (see ESI†). The current–voltage (*I–V*) relationship of the fabricated device has been studied in the dark as well as under irradiation (intensity ~100 mW cm^{-2}) conditions at room temperature (300 K) and at the corresponding applied bias voltage sequentially within the limit ±1 V to analyze the charge transport behaviour. All studies were carried out in a N_2 filled glove box and at a laboratory temperature of 26 °C.

The *I–V* characteristics of the Cr-based device have been recorded under dark and irradiation conditions (Fig. 3). Under dark conditions, the electrical conductivity of the device has been estimated as 1.40×10^{-2} S m^{-1}, typical of a semiconductor. However, once exposed to photoirradiation, the conductivity of the same device has been estimated as 1.61×10^{-2} S m^{-1}. It is clear that the conductivity of the device improves considerably under irradiation conditions compared to that under non-irradiation conditions.

Besides, the illustrative *I–V* characteristics of the Al/metallogel based interface under both dark and photo-illumination conditions (Fig. 3) reveal a nonlinear rectifying behaviour,

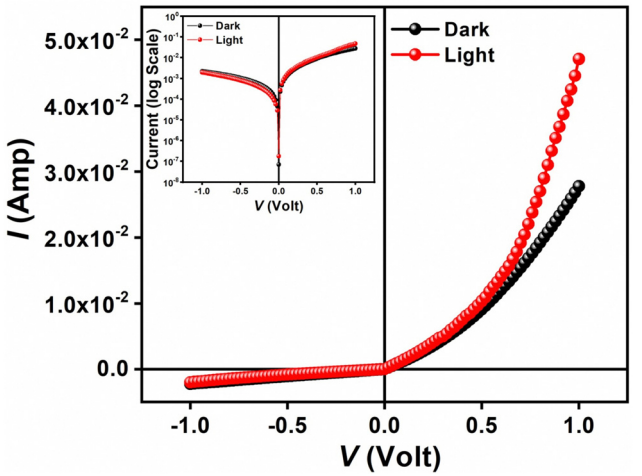

Fig. 3 *I–V* characteristics curve of the gel/Al structured thin film device under dark and photo-illumination conditions.

similar to the Schottky diode (SD). Under photo-illumination conditions, our material based device exhibits a larger current which indicates its photosensitivity. Accordingly, we measure the photosensitivity of our device, which turns out to be 0.70.

Furthermore, the thermionic emission theory was used to analyze the obtained *I–V* characteristics of the Cr-based SD. In this regard Cheung's method has also been employed to extract important diode parameters[49–53] (eqn (S1)–(S7), ESI†).

The ideality factor (η) and the series resistance (R_S) of our fabricated device have been calculated (Table 1) from the intercept and the slope of the dV/d ln I *vs.* I plot (Fig. 4(a) and (b)) under both dark and irradiation conditions. The calculated value of the ideality factor (η) of the fabricated SD shows deviations from its ideal value of 1 and has been estimated as 0.72 and 0.82 under dark and irradiation conditions, respectively. The existence of interface states and series resistance at the junction and the presence of inhomogeneities of the Schottky barrier height may be mainly attributed to such nonideal behaviour.[52,54]

However, under photo-illumination conditions the ideality factor of the fabricated SD approaches a more ideal value (closer to 1), which is a significant observation. This observation reveals the reduced recombination of interfacial charge carriers and the generation of a better homogeneity at the barrier of Schottky junctions. From this analysis, it may be concluded that the synthesized gel based SD possesses fewer carrier recombination centers at the junction, *i.e.* a better barrier homogeneity even under irradiation conditions.

In order to get a better insight into the barrier homogeneity, we have calculated the value of barrier height (ϕ_B) from the intercept of the $H(I)$ *vs.* I plot (Fig. 4(a) and (b), using eqn (S6), ESI†). The barrier potential height of the device shows a reduction under irradiation conditions. This reduction may occur due to the accumulation of the produced photo-induced charge carriers near the conduction band. The slope of the $H(I)$ *vs.* I plot also gives the series resistance (R_S). The measured potential heights (ϕ_B), ideality factors (η) and series resistances (R_S) under dark and illumination conditions for the metal (Al)–semiconductor (Cr-based gel material) (MS) junction are tabulated in Table 1. The obtained value of R_S for both processes show an excellent regularity. The diminution of the R_S of our device due to exposure to irradiation signifies its applicability in the field of optoelectronics.

For an in-depth analysis of the charge transport phenomena at the MS junction, we have further studied the *I–V* curves. The characteristic *I–V* curves under both conditions on the logarithmic scale reveal that they can be differentiated into two regions (region I and region II) having different slope values (Fig. 4(c) and (d)).

The first region (region-I), with a slope value of ~ 1, symbolizes the Ohmic regime, wherein the generated current follows a simple relation of $I \propto V$. On the other hand, the portion where the current is proportional to V^2 is marked as the second region (region-II) (Fig. 4(c) and (d)). However, a characteristic slope value of *ca.* 2 indicates a trap free space charge limited current (SCLC) regime.[49,55] It is noteworthy here that when the injected carriers are more than the background carriers, the injected carriers spread and generate a space charge field. In this region the current is controlled by this space charge field and is known as the SCLC[49,55] and it is as such adopted here to estimate device performance.

Following this model, the effective carrier mobility has been estimated from the higher voltage region of the I *vs.* V^2 plot (Fig. 4(e)) using the Mott–Gurney equation:[49,52,55]

$$I = \frac{9\mu_{\text{eff}}\varepsilon_0\varepsilon_r A}{8}\left(\frac{V^2}{d^3}\right) \quad (2)$$

where I, ε_0, ε_r, and μ_{eff} are the current, permittivity of free space, relative dielectric constant of the synthesized material and effective mobility, respectively.

The relative dielectric constant has been estimated as 8.02, measured from the plot of capacitance against frequency (C *vs.* f) for the Cr-based film at a constant bias potential (Fig. 4(f)) by using the equation:

$$\varepsilon_r = \frac{Cd}{\varepsilon_0 A} \quad (3)$$

where ε_0 is the free space permittivity, d is the thickness of the film, A is the area of the diode, and C is the capacitance of the material.

Capacitors exhibit a property called capacitive reactance (X_c), which is inversely proportional to frequency (f). The formula of

Table 1 Schottky device parameters of the Cr-based diode

Condition	Conductivity (S m^{-1})	Photosensitivity	Ideality factor (η)	Barrier height (eV)	R_S from dV/d ln I (Ω)	R_S from H (Ω)
Dark	1.40×10^{-2}	0.70	0.72	0.88	62.43	62.03
Light	1.61×10^{-2}		0.82	0.73	55.70	57.04

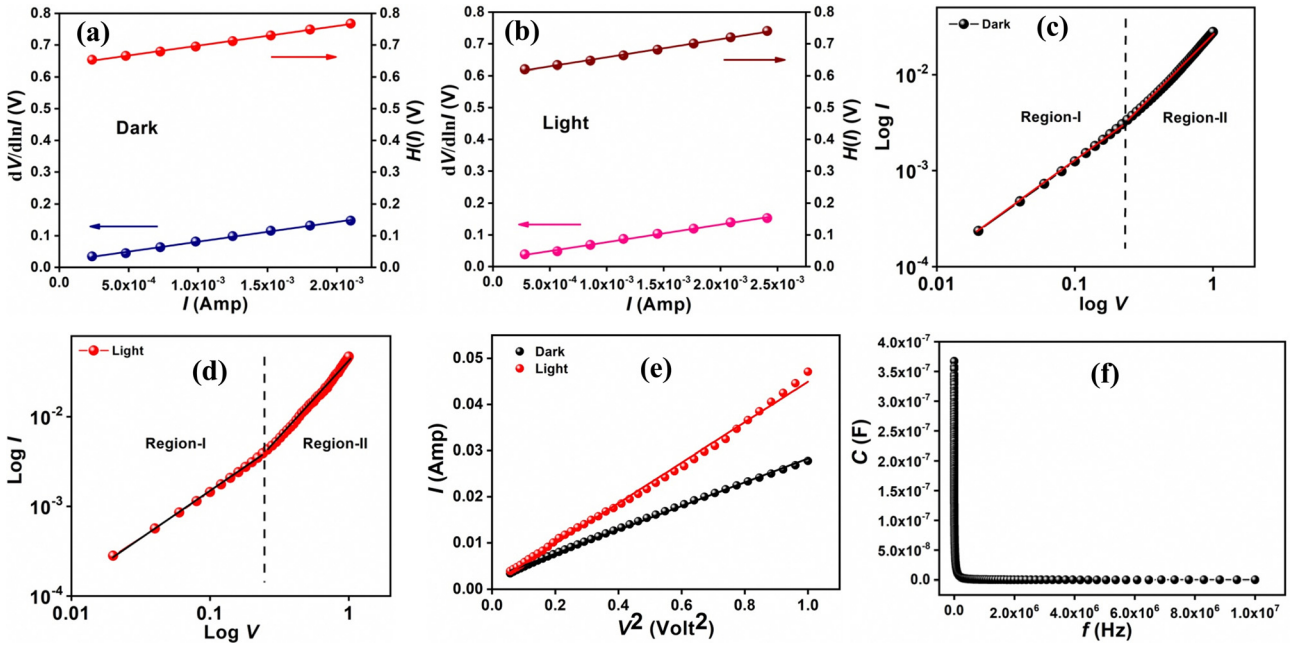

Fig. 4 The electrical data showing (a) and (b) $dV/d\ln I$ *vs.* I and $H(I)$ *vs.* I curves, (c) and (d) $\log I$ *vs.* $\log V$ curves, (e) I *vs.* V^2 curves for the synthesized Cr-based thin film device under dark and irradiation conditions and (f) the capacitance *vs.* frequency graph for the determination of the dielectric constant.

capacitive reactance is $X_c = 1/(2\pi fC)$, where C is the capacitance. As frequency increases, the capacitive reactance decreases, which means that the effective impedance of the capacitor decreases, resulting in decreased capacitance at higher frequencies.

Furthermore, the transit time (τ), an important parameter to analyze charge transport across the junction, was calculated from the slope of the SCLC region (region-II), as shown in Fig. 4(c) and (d), using the following equation:[56]

$$\tau = \frac{9\varepsilon_0\varepsilon_r A}{8d}\left(\frac{V}{I}\right) \quad (4)$$

All parameters estimated in the SCLC region demonstrate that the charge transport properties of the material improve under illumination conditions (Table 2). The higher mobility implied a higher transport rate under irradiation, while the number of charge carriers also increased under the same conditions. The diode parameters of the synthesized complex based SD demonstrate superior charge transfer kinetics under irradiation conditions. So, these kinds of materials can pave the way for a very promising future in device applications.

To check the stability of the nanocomposite gel/Al structured thin film we have done the measurement at time intervals of 24, 48 and 72 h. We obtained almost the same pattern and results with the highest current values of 2.78×10^{-2} amp, 3.16×10^{-2} amp, and 2.94×10^{-2} amp respectively. So, we can conclude that the nanocomposite gel/Al structured thin film is stable. The corresponding current–voltage characteristic graph is shown in the ESI† (Fig. S6).

Table 2 Charge conducting parameters of Cr-based thin film devices

Condition	ε_r	μ_{eff} ($m^2\ V^{-1}\ s^{-1}$)	τ (s)	$\mu_{eff}\tau$ ($m^2\ V^{-1}$)
Dark	2.52	1.45×10^{-4}	7.80×10^{-10}	1.131×10^{-13}
Light		2.47×10^{-4}	4.65×10^{-10}	1.148×10^{-13}

The azide-functionalized metallogel for proton conductivity measurements

Interestingly, the azide-functionalized metallogel provides us with a unique opportunity to explore the role of immobilized functionalities, which can exist as distinctly charge-separated resonance structures, in improving proton conductivity, the most important parameter required for an efficient fuel cell membrane.[57,58] Accordingly, detailed proton conductivity experiments were carried out on a xerogel sample using alternating current (ac) impedance spectroscopy under variable temperature and relative humidity conditions. As illustrated in the inset of Fig. 5(a), an equivalent circuit model comprising bulk resistance (R_b), a capacitor (C_1) and Warburg impedance (Z_w) has been used for the analysis of the impedance data. Subsequently, EIS-analyzer software was utilized for fitting the impedance plots. Based on the above circuit model, the proton conductivity (σ_p) values from the bulk resistance (R_b) are calculated by using the following equation:

$$\sigma_p = \frac{1}{R_b}\left(\frac{t}{A}\right) \quad (5)$$

where t represents the thickness (the distance between two SS electrodes) and A represents the area of the SS electrode covered by the xerogel, respectively.

The as-synthesized xerogel sample turns out to be reasonably conductive in nature and shows a proton conductivity value of 3.35×10^{-6} S cm^{-1} at 30 °C. Two major factors that dictate the conductivity values are (i) the availability of the

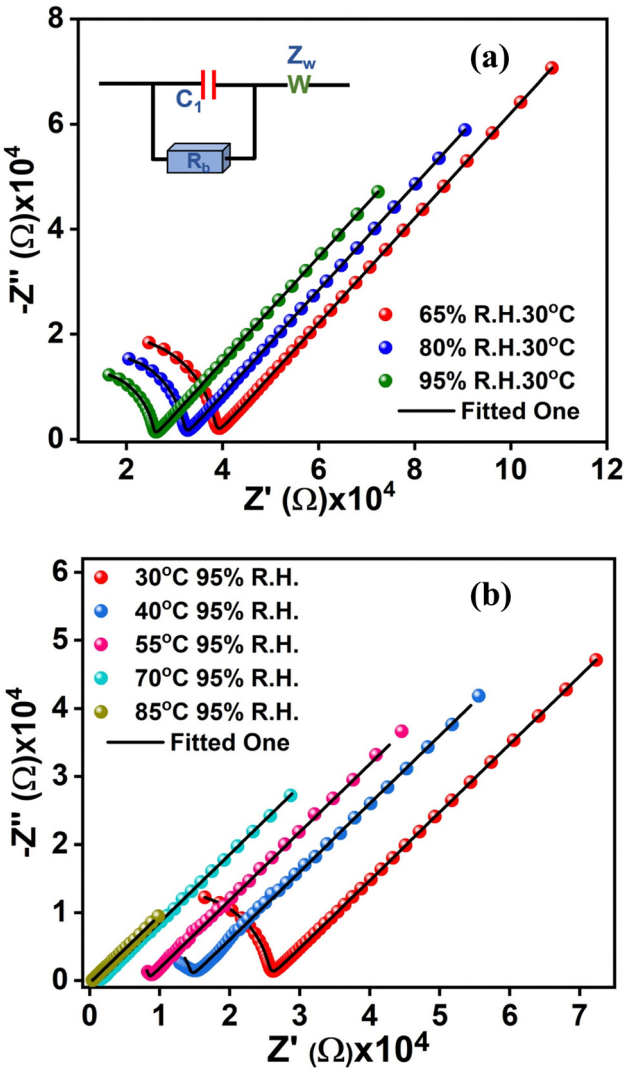

Fig. 5 The Nyquist plots of the xerogel at different conductivities collected at (a) different relative humidities at a fixed temperature of 30 °C. (inset) The impedance data were analysed with an equivalent circuit model, where C_1, Z_w, and R_1 represent the capacitance, Warburg impedance and bulk resistance, respectively and (b) different temperatures at a fixed R.H. of 95%.

charged particles (H^+) which are more often than not sourced from the externally supplied steam and (ii) the transportation of the charged particles. While relative humidity can play a major role in sourcing the charged particles, their transportation,[59] on the other hand, can greatly be influenced by temperature.[60] Naturally, a detailed proton conductivity study was performed by systematically varying temperature and relative humidity. In the present case, the metallogel does not show any significant enhancement in proton conductivity values with RH. With variable RH (at a fixed temperature of 30 °C) proton conductivity values are estimated as 3.35×10^{-6} at 65% RH, 4.03×10^{-6} at 80% RH and 5.03×10^{-6} at 95% RH (Fig. 5(a) and Table 3). The conductivity, however, exhibits a temperature-dependent (at a fixed R.H. of 95%) upward trend while the best value for the metallogel was estimated as 3.30×10^{-4} S cm^{-1} at 85 °C (Fig. 6(a)). The results are comparable with a similar class of coordination polymer based gel systems as well as other crystalline MOFs and coordination polymers. Furthermore, the xerogel network remained intact, which was confirmed by matching the IR spectra taken before and after the above conductivity measurements (Fig. S7, ESI†).

Table 3 Proton conductivity values of the xerogel at different temperatures and humidities

Relative humidity (%)	Temperature (°C)	Conductivity (S cm^{-1})
65	30	3.35×10^{-6}
80		4.03×10^{-6}
95		5.03×10^{-6}
95	40	9.71×10^{-6}
	55	1.55×10^{-5}
	70	8.75×10^{-5}
	85	3.3×10^{-4}

Determination of the mechanism and activation energy of proton conduction

Generally, the proton conduction process follows two types of mechanisms, the Grotthuss mechanism and vehicle mechanism. In the Grotthuss mechanism, the first step involves the generation of charge gradients among hydrogen bonded water molecules and solvents which subsequently led to charged species separation in terms of H^+. In the next step, the protons hop from one site to another site of the extended hydrogen bonded network with a few local rearrangements. In the vehicle mechanism, protons use entrapped solvent molecules as vehicles that assist in the transportation of the charged species through diffusion. Interestingly, the mechanism of proton conduction can be determined quantitatively by estimating the activation energy value of the said process. The rule of thumb is that the activation energy in the range 0.1–0.4 eV implies the Grotthuss mechanism, whereas the activation energies of 0.4 eV and above imply the vehicle mechanism.[61,62]

The activation energy (E_a) of a process can be estimated from the proton conductivity (σ_P) values at different temperatures using the following Arrhenius equation:

$$\sigma_p T = \sigma_0 \exp\left(\frac{-E_a}{k_B T}\right) \quad (6)$$

where σ_0 is the pre-exponential factor, E_a is the activation energy, k_B is the Boltzmann constant, and T is the absolute temperature.

Eqn (4) can be restructured into a straight-line equation in the following manner:

$$\ln(\sigma_p T) = \ln \sigma_0 - (E_a/k_B T) \quad (7)$$

Subsequently, with the help of the straight-line fits of $\ln(\sigma_p T)$ and $1000/T$, the value of E_a can readily be calculated from the slope of the line (Fig. 6(b)). Using the above method, the calculated activation energy of the current xerogel turns out to be 0.743 eV. As the E_a value of the process is >0.4 eV we can conclude that the proton conduction in the xerogel follows the vehicle mechanism.

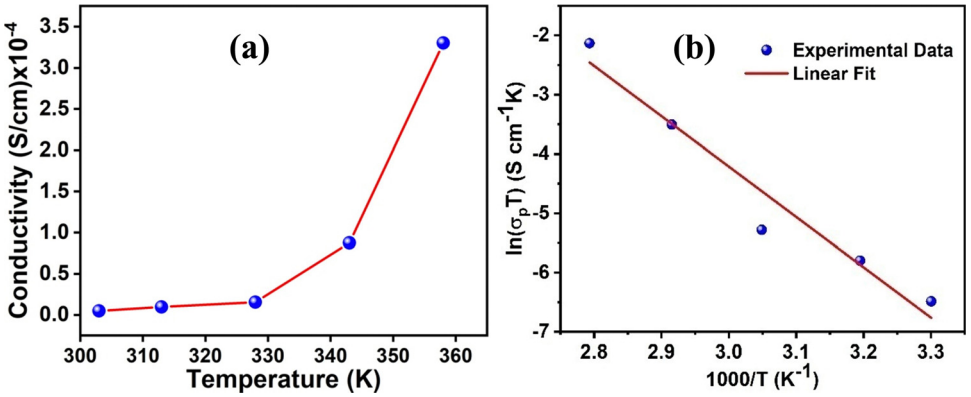

Fig. 6 (a) The proton conductivity results of the metallogel showing a variable temperature proton conductivity trend at a fixed R.H. of 95% and (b) Arrhenius plot for activation energy estimation.

Considering the coordination polymer based Cr(III) gel, we found some intrinsic hydroscopic nature of the xerogel which is evident from TGA data (Fig. S5, ESI†). Further support comes from the ability of the azide group grafted to the pores of the network (since it shows selective CO_2 adsorption) to hold the water molecules which are the proton source. To confirm this, we subsequently activated the xerogel through solvent exchange with CH_3CN followed by heating to have a material supposed to be devoid of entrapped H_2O molecules. From the impedance data and Nyquist plot (Fig. S8a, ESI†) the conductivity was found to be 2.89×10^{-8} S cm^{-1} under ambient conditions which is considerably lower as compared to the reported value. Besides, unlike the reported data, the nature of the semicircular path (Fig. S8a, ESI†) indicates the poor conducting nature of the material. Therefore, to the best of our knowledge there must be a H^+ conduction pathway (Fig. S8b, ESI†) present in the system.

Magnetic metallogels

One of the major advantages of a metallogel is that the introduction of a metal not only strengthens the chassis of the porous network but also incorporates many metal-specific physicochemical properties into the system.[63] Of particular interest is magnetism. Furthermore, recent studies have highlighted the manifold advantages of magnetic adsorbents over conventional systems.[64] Chromium being a first row transition metal, with a d^3 (Cr^{3+}) electronic configuration, is expected to form a magnetic metallogel and prompted us to explore the magnetic behavior of the resultant gel.

A thorough magnetic study of the xerogel was performed in order to investigate the magnetic behavior of the metallogel material. A DC magnetic susceptibility plot is shown in the form of $\chi_g T$ (χ_g = gram magnetic susceptibility) *vs.* T (Fig. 7(a)). At room temperature, the $\chi_g T$ value is 2.62 cm^3 g^{-1} K. As the temperature is lowered down, the $\chi_g T$ value also gradually decreases, probably due to antiferromagnetic interactions.

$1/\chi_g$ *vs.* T was plotted in the temperature range of 20–300 K and fitted with the Curie–Weiss equation, $1/\chi_g = (T - \theta)/C$ (Fig. 7(b)). From the fitting, $C = 3.23$ cm^3 g^{-1} K and $\theta = -69.7$ K were obtained. The C value is close to the $\chi_g T$ value at room temperature. A negative value of θ suggests indeed antiferromagnetic interactions present in the network with adjacent chromium centres. To further check any magnetic ordering like behavior, an isothermal magnetization curve was plotted at 2 K. However, no hysteresis loop was found (inset, Fig. 7(a)).

Magnetic metallogels as porous adsorbents

Metallogels are associated with a couple of intrinsic features that perfectly overlap with the prerequisites of an adsorbent

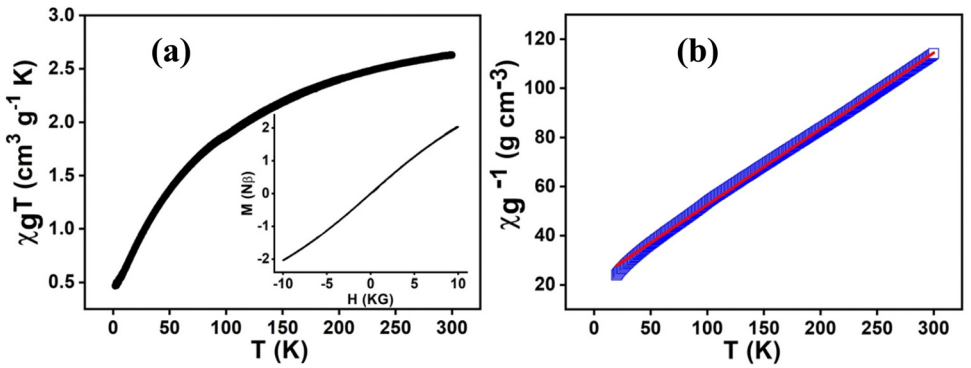

Fig. 7 Magnetic data of the xerogel showing (a) the DC magnetic susceptibility plot (inset: the $M/N\beta$ *vs.* H plot of the freshly prepared xerogel at 2 K) and (b) the $1/\chi_g$ *vs.* T plot.

material, *viz.*, a porous network and the presence of immobilized functional groups on the surface of the material that can facilitate the direct interaction with the guest or solvent molecules. It is well known that adsorption capability is directly proportional to the surface area, which is again related to the size of the material. In the present case, morphological studies indicate the enhanced adsorption capability of the Cr–metallogel. The smaller size (10–50 nm) of the NMOPs of the metallogel will enhance the effective surface area. Furthermore, it will provide more interparticle cross-linking sites in the network, which can effectively interact and entrap the guest molecule and therefore enhance the adsorption capability of the metallogel.

In order to check and quantify the porous nature of the Cr–metallogel, detailed gas sorption studies have been carried out. The sorption studies were carried out using the corresponding xerogel. The idea is to remove the entrapped solvent molecules, while keeping the intrinsic porous network intact. The N_2 adsorption measured at 77 K shows a N_2 uptake of $\sim$24 cc g^{-1} (Fig. S9a, ESI†) with a BET surface area of 7.6 m^2 g^{-1}. A Barrett–Joyner–Halenda (BJH) adsorption average pore diameter of 29.6 nm suggests a characteristic mesoporous feature of the xerogel. Since N-rich functional groups have a special affinity towards CO_2, we further extended our adsorption experiments in order to understand the role of the azide ($-N_3$) functional group present in the gel network in CO_2 adsorption. The CO_2 adsorption was measured at room temperature within a relative pressure range of 0 to 1 atm. An adsorption of $\sim$12 cc g^{-1} of CO_2 at room temperature is a considerably high value for a xerogel system. However, the xerogel absorbs poor amounts of both N_2 (approx. 3 cc g^{-1}) and CH_4 (approx. 5 cc g^{-1}) at room temperature indicating the fact that the material shows selectivity towards CO_2 adsorption at room temperature (Fig. S9b, ESI†).

Toxic dye adsorption and release

The above results unequivocally confirm the magnetic-adsorbent nature of the as-prepared Cr-metallogel. The next obvious question then arose as to whether a similar adsorption ability of the xerogel could be reproduced with toxic organic dyes as guest molecules. In order to find an answer to the above question, we carried out detailed adsorption studies with the three most commonly used water soluble organic dyes, methylene blue (MB), rhodamine B (RhB) and crystal violet (CV). Investigations were carried out using 1.5×10^{-5} (M) MB, 1.0×10^{-5} (M) RhB and 1.5×10^{-5} (M) CV aqueous solutions because of their comparable absorbance intensities. In a typical experiment, each dye solution was treated separately with 10 mg of the freshly prepared xerogel. It was gratifying to note that all experiments showed a general trend of gradual decrease in the intensities of colours with time (Fig. S10, ESI†), signifying the dye adsorption by the chromium based metallogel. The as-prepared metallogel was found to be highly effective in dye adsorption, with an adsorption-assisted decolourization percentage of 80% within 2 hours. In order to quantify the adsorption behaviour, the time-dependent changes in intensities were studied using UV-Vis spectroscopy. Accordingly, the intensities of the characteristic absorption peaks, at 665 nm for MB, at 570 nm for RhB and at 600 nm for CV, were recorded periodically using a UV-Vis spectrometer (Fig. 8(a)–(c)).

Subsequently, the adsorption-assisted removal of the dyes from the solutions in terms of percentage (Fig. 9(a)) is

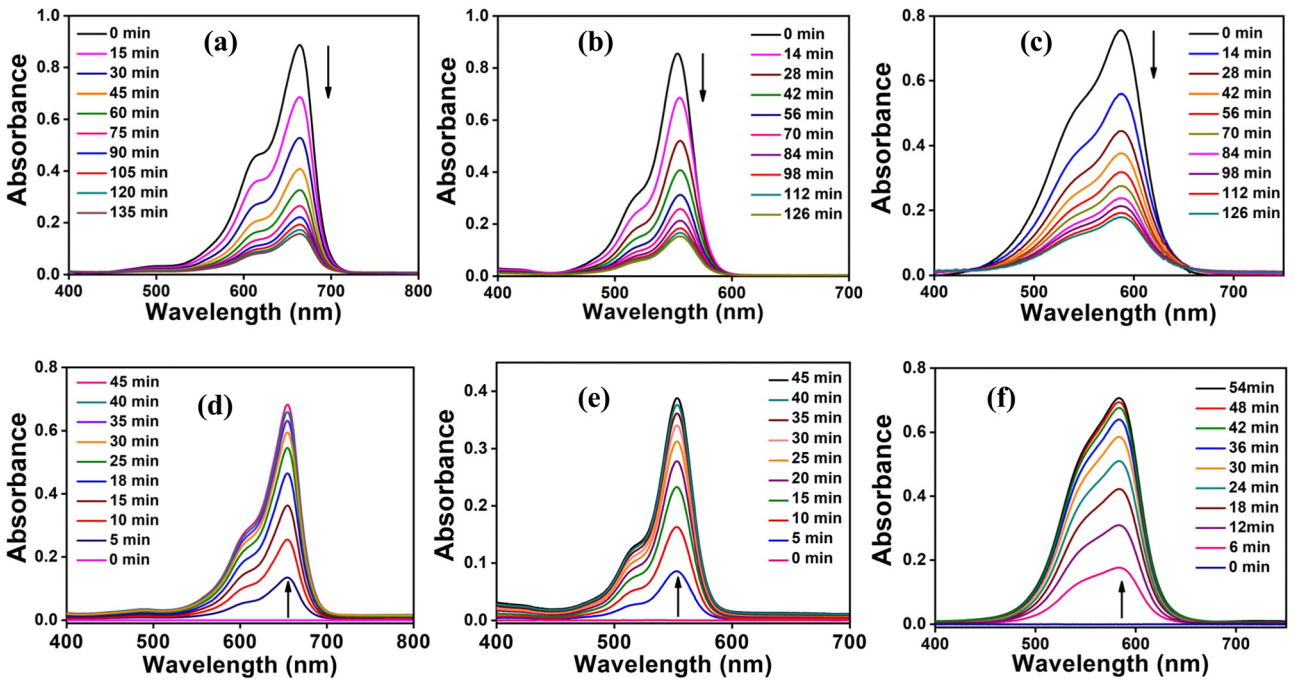

Fig. 8 Time-dependent UV-Vis spectra of (a) MB, (b) RhB and (c) CV showing the gradual change in intensity due to adsorption and (d), (e), (f) are the time-dependent UV-Vis spectra of MB, RhB and CV respectively showing the gradual change in intensity due to release in ethanol.

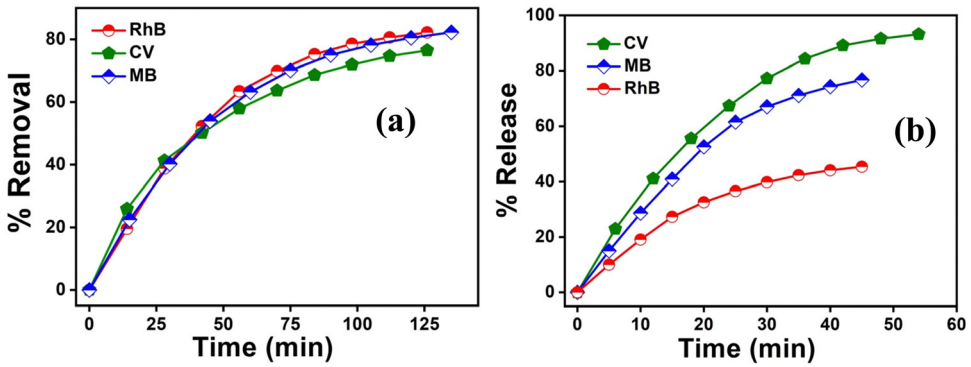

Fig. 9 (a) % Removal of dyes and (b) % release of dyes.

calculated using the following formula:

$$\%\text{Removal} = \frac{C_0 - C_t}{C_0} \times 100\% \quad (8)$$

where C_0 is the concentration of dye (in aqueous medium) taken for adsorption and C_t is the concentration of dye at a particular time (t).

As illustrated in Table S2 (ESI†), the as-prepared xerogel was found to remove more or less 80% of the dyes from all their respective aqueous solutions. The IR (Fig. S11a, ESI†) spectrum of each dye-soaked xerogel matches with the xerogel itself which proves that there is no change in the chemical properties of the xerogel. Hence, it is a clear case of nothing but the adsorption of dyes over the available surface of the xerogel.

The above experimental results nicely demonstrate the effectiveness of the Cr-gel as a magnetic adsorbent for potential application in wastewater purification. Furthermore, inspired by recent trends in the re-use of the dye molecules, we also carried out a detailed investigation of the release, or more specifically, the desorption of the adsorbed dye molecules from the as-prepared Cr-gel. Typical preliminary screenings were done by simply soaking the dye-loaded xerogels in different solvent systems. The gradual increase in the intensity of the characteristic colours confirms the release of the organic dyes (Fig. S10, ESI†).

Ethanol turned out to be the best solvent system. Again, time-dependent changes in intensities were studied using UV-Vis spectroscopy to quantify the release of the dye molecules. Similar to removal experiments, the intensities of the characteristic absorption peaks, at 665 nm for MB, at 570 nm for RhB and at 600 nm for CV, were recorded periodically using a UV-Vis spectrometer (Fig. 8(d)–(f)). The absorption intensities for the dye release experiment were collected till they reach a saturation point with no further increase in intensity. The release of dyes in ethanol in terms of percentage (Fig. 9(b)) is calculated using the following formula:

$$\%\text{Release} = \frac{C_{\text{rel.}}}{C_{\text{ads.}}} \times 100\% \quad (9)$$

where $C_{\text{rel.}}$ is the concentration of dye (in ethanol) at the respective time of release and $C_{\text{ads.}}$ is the concentration of dye at the start of adsorption.

As illustrated in Table S2 (ESI†), the recovery rate of CV was as high as 93%. Finally, the reusability of the Cr-gel was crosschecked by washing it several times with water–ethanol solution. The recycled dye-free Cr-gel was equally potent in adsorbing and desorbing a fresh batch of dye molecules. There were no significant changes in the IR spectra (Fig. S11b, ESI†) as recorded after each case of release. The adsorption/desorption process (Fig. S12, ESI†) can be repeated several times without any loss of activity of the xerogel.

Conclusion

The aim of the present investigation was to develop a coordination polymer based metallogel system showing mutually inclusive electrical and magnetic properties. Accordingly, we have successfully developed a Cr-metallogel using 5-azido isophthalic acid as a linker-cum-gelator molecule. The metallogel resulted from the not-so-common aggregation of numerous spherical NMOPs and showed very high gel strength as well as self-healing, self-sustaining, and thixotropic properties. The exploration of the electrical properties of the metallogel supports its candidature as a proton conductivity based fuel cell membrane and Schottky barrier diode formation. The photosensitivity of our device turns out to be 0.70 and it is an excellent light-dependent diode with ideality factors of 0.72 (in the dark) and 0.82 (in the presence of light), while the corresponding conductivity values are 1.40×10^{-2} S m^{-1} (dark) and 1.61×10^{-2} S m^{-1} (light). Further support for potential electrical device fabrication comes from proton conductivity experiments. The free immobilized azide group, featuring in-built charge-separated resonance structures, acts as a proton carrier facilitator-cum-transporter and shows an impressive proton conductivity value of 3.3×10^{-4} S cm^{-1} at 95% relative humidity and 85 °C. Furthermore, the as-prepared porous magnetic metallogel was utilized for toxic organic dye removal from wastewater. Its antiferromagnetic behaviour was confirmed by DC magnetic susceptibility data. On the other hand, the interesting selective CO_2 gas sorption data further corroborate the adsorbent nature of the metallogel. Furthermore, the release of the adsorbed dye molecules from the gel-matrix confirms the recovery and re-use of the dye molecules. To the

best of our knowledge, this kind of tandem-arrayed chromium-gel based wastewater treatment technique has not been reported hitherto in the literature but has a huge potential application in magnetic adsorbent based environmental remediation.

Experimental

Materials and general methods

All chemicals were purchased (Aldrich) and used without further purification. FT-IR spectra were recorded on a Nicolet MAGNA-IR 750 spectrometer with the KBr pellet-containing samples. Thermal analysis was carried out with a TA Instruments SDT Q600 instrument under a nitrogenous atmosphere with a flow rate of 100 mL min^{-1}. Mass spectra were collected from a Micromass Q-Tof Micro instrument. The elemental analyses were carried out using a PerkinElmer 2400 Series-II CHN analyzer with the accuracy of C, H, and N determination being better than 0.30% abs. Magnetic data of the xerogel sample were collected using an MPMS SVSM (MPMS-3) provided by Quantum Design with $\leq$10–8 emu sensitivity.

Gelation test

To 10 mg of the ligand dissolved in 0.5 ml of MeOH kept in a screw-capped sample vial, was added 0.5 ml of the $Cr(NO_3)_3$ (1 wt% 1 eq. ligand–metal ratio) solution in DMF. The mixture was kept at 80 °C in an air oven for 7–8 h. A bottle green coloured gel was obtained which was confirmed by a 'stable-to-inversion of the vial' test method. The IR spectra (Fig. S1, ESI†) were collected for the xerogel.

IR (400–4000 cm^{-1}): 3415b, 2969b, 2779m, 2439w, 2113s, 1587w, 1384b, 1193w, 1022m, 825m, 775m, 721m, 669w, 540w, 516w.

Rheological studies

Rheological experiments were done with an Antor Paar Compact Modular Rheometer (MCR 102) with high sensitivity (from 7.5 nN m to 2 nN m). A parallel plate measuring system (PP 25) with a diameter of 40 mm was used. The distance between the system and the plate was adjusted so as to remove any air gap between them. The gel was prepared freshly and transferred on the plate and all rheological experiments were done on the gels at a constant temperature of 25 °C.

SEM studies

A little amount of gel sample was placed on a clean glass slide and then it was dried by the slow evaporation of solvents. The material was then dried under vacuum at 30 °C for 2 days. The material was silver-coated, and the micrographs were taken using FESEM apparatus Carl Zeiss AG SUPRA 55 VP-41-32 with a resolution of 1.0 nm at 15 kV.

TEM studies

A little amount of sample was added into 1 ml of 1 : 1 DMF–MeOH in a glass vial and the mixture was sonicated for a few hours. Then 1 drop of the solution was drop cast on a 300 mesh carbon-coated copper grid, dried under vacuum and mounted on a JEOL JEM 2010 high-resolution microscope instrument with a point resolution of 0.19 nm for TEM imaging and operating at an accelerating voltage of 200 kV.

Spectral studies

For FTIR studies spectra were collected with samples prepared as KBr pellets. UV-Visible studies were performed on a CARY 100 Bio UV-Vis spectrophotometer (wavelength(s): 190 to 900 nm, light source: tungsten halogen) with an accuracy of $\pm$2 nm, taking 2.5 $\times$ 10^{-5} (M) ligand solution prepared using 1 : 1 DMF/MeOH solution. 10 mg of the gel was dissolved in 10 mL of a DMF/MeOH mixture and diluted 5 times to get the spectra.

BET measurements

The freshly prepared xerogel was activated prior to its adsorption experiments. For activation, 200 mg of the xerogel was dipped in 30 ml of a 1 : 1 DCM–MeOH mixture and kept for 24 h under stirring conditions so as to get rid of high boiling solvents like DMF trapped in the pores. After solvent exchange the material was filtered and was heated in a vacuum at 80 °C for another 12 h. After that the xerogel was degassed for 24 h at a target temperature of 80 °C followed by N_2 adsorption at 77 K using a Micromeritics ASAP 2020 adsorption analyzer with an accuracy within 0.15% of reading.

SBD device fabrication

For the fabrication of the Al–Cr Schottky device, an indium tin oxide (ITO) coated glass substrate was cleaned with acetone, distilled water, and isopropanol repeatedly and sequentially in an ultrasonication bath for 20 min. At the same time, a well-dispersed solution of the complex salt in the *N*,*N*-dimethylsulfoxide (DMSO) medium was prepared and spin-coated onto the pre-cleaned ITO coated glass at 600 rpm for 1 min employing an SCU 2700 spin coating unit. The spin coating was repeated another 4 times. Thereafter, it was dried in a vacuum. The thickness of the film was measured using a surface profiler and calculated as 1 μm. The aluminum (Al) electrodes were deposited onto the film using a vacuum coating unit (12A4D of HINDHIVAC) at a pressure of 10^{-6} torr. The area of the Al electrodes was maintained as 7.065 $\times$ 10^{-6} m^2 using a shadow mask. The current–voltage measurements of the fabricated device employing the complex salts (**1** and **2**) were carried out using a Keithley 2635B source meter (accuracy is the same as the current source: $<\pm$(0.1% + 10 mV) typical) interfaced with a PC under dark conditions in the voltage range of −1 V to +1 V at room temperature.

Solid state proton conductivity experiments

Almost 150 mg of the powdered Cr based xerogel was sandwiched between two carbon paper sheets after pelletizing the sample by maintaining 5 ton cm^{-2} pressure in a hydraulic press for 2 min. Carbon papers have the ability to reduce the contact resistance between the electrodes and sample. After the

pelletization process was completed, the diameter and thickness were measured cautiously. The diameter of the pellet is around 1 cm and the thickness is around 0.1 cm. The sandwiched pellet was then put between two probe electrodes (electrode||sample||electrode) made of stainless steel. An alternating current electrochemical impedance spectroscopy workstation was used for performing proton conductivity experiments. The spectra were recorded by applying a 100 mV DC potential, in the frequency range of 1 Hz to 1 MHz. Our homemade humidity chamber was used to maintain specific temperature and humidity. To specifically adjust to certain conditions, 8 hours of time was given between each measurement. During low humidity experiments (at 65% RH), the pelletized sample was kept in a humidity box under specified conditions for 6 hours prior to each measurement. A CH Instruments electrochemical workstation (with 16-bit resolution, 0.003% accuracy) operated using its own software was used for impedance spectroscopy data collection. After that, EIS-analyser software was used for fitting the data with appropriate electrical circuits to get conductivity values.

Conflicts of interest

There are no conflicts to declare.

Acknowledgements

RM gratefully acknowledges the Department of Science and Technology (DST), India, for financial assistance (project no. DST/INT/SWD/VR/P-05/2019).

References

1 N. J. Szymanski, Y. Zeng, H. Huo, C. J. Bartel, H. Kim and G. Ceder, Toward autonomous design and synthesis of novel inorganic materials, *Mater. Horiz.*, 2021, **8**, 2169–2198.
2 J. Liu, A. M. Kaczmarek and R. V. Deun, Advances in tailoring luminescent rare-earth mixed inorganic materials, *Chem. Soc. Rev.*, 2018, **47**, 7225–7238.
3 S. Bala, S. Akhtar, J.-L. Liu, G.-Z. Huang, S.-G. Wu, A. De, K. S. Das, S. Saha, M.-L. Tong and R. Mondal, Fascinating interlocked triacontanuclear giant nanocages, *Chem. Commun.*, 2021, **57**, 11177–11180.
4 S. Singh, H. Chen, S. Shahrokhi, L. P. Wang, C.-H. Lin, L. Hu, X. Guan, A. Tricoli, Z. J. Xu and T. Wu, Hybrid Organic-Inorganic Materials and Composites for Photoelectrochemical Water Splitting, *ACS Energy Lett.*, 2020, **5**, 1487–1497.
5 A. De and R. Mondal, Toxic Metal Sequestration Exploiting a Unprecedented Low Molecular-Weight Hydrogel-to-Metallogel Transformation, *ACS Omega*, 2018, **3**, 6022–6030.
6 B. O. Okesola and D. K. Smith, Applying low-molecular weight supramolecular gelators in an environmental setting – selfassembled gels as smart materials for pollutant removal, *Chem. Soc. Rev.*, 2016, **45**, 4226–4251.
7 D. J. Cornwell and D. K. Smith, Expanding the scope of gels – combining polymers with low-molecular-weight gelators to yield modified self-assembling smart materials with high-tech applications, *Mater. Horiz.*, 2015, **2**, 279–293.
8 S. Basak, S. Bhattacharya, A. Datta and A. Banerjee, Charge-Transfer Complex Formation in Gelation: The Role of Solvent Molecules with Different Electron-Donating Capacities, *Chem. – Eur. J.*, 2014, **20**, 5721–5726.
9 V. Gabrielli, R. Baretta, R. Pilot, A. Ferrarini and M. Frasconi, Insights into the Gelation Mechanism of Metal-Coordinated Hydrogels by Paramagnetic NMR Spectroscopy and Molecular Dynamics, *Macromolecules*, 2022, **55**, 450–461.
10 R. Xing, K. Liu, T. Jiao, N. Zhang, K. Ma, R. Zhang, Q. Zou, G. Ma and X. Yan, An Injectable Self-Assembling Collagen–Gold Hybrid Hydrogel for Combinatorial Antitumor Photothermal/Photodynamic Therapy, *Adv. Mater.*, 2016, **28**, 3669–3676.
11 J. Song, C. Yuan, T. Jiao, R. Xing, M. Yang, D. J. Adams and X. Yan, Multifunctional Antimicrobial Biometallohydrogels Based on Amino Acid Coordinated Self-Assembly, *Small*, 2020, **16**, 1907309.
12 J. Bai, R. Wang, X. Wang, S. Liu, X. Wang, J. Ma, Z. Qin and T. Jiao, Biomineral calcium-ion-mediated conductive hydrogels with high stretchability and self-adhesiveness for sensitive iontronic sensors, *Cell Rep. Phys. Sci.*, 2021, **2**, 100623.
13 S. Bhattacharya, S. Sengupta, S. Bala, A. Goswami, S. Ganguly and R. Mondal, Pyrazole-Based Metallogels Showing an Unprecedented Colorimetric Ammonia Gas Sensing through Gel-to-Gel Transformation with a Rare Event of Time-Dependent Morphology Transformation, *Cryst. Growth Des.*, 2014, **14**, 2366–2374.
14 A. Y.-Y. Tam and V. W.-W. Yam, Recent advances in metallogels, *Chem. Soc. Rev.*, 2013, **42**, 1540–1567.
15 S. Dhibar, A. Dey, D. Ghosh, S. Majumdar, A. Dey, P. P. Ray and B. Dey, Triethylenetetramine-Based Semiconducting Fe(III) Metallogel: Effective Catalyst for Aryl−S Coupling, *ACS Omega*, 2020, **5**, 2680–2689.
16 J. H. Jung, J. H. Lee, J. R. Silverman and G. John, Coordination polymer gels with important environmental and biological applications, *Chem. Soc. Rev.*, 2013, **42**, 924–936.
17 B. S. Luisi, K. D. Rowland and B. Moulton, Coordination polymer gels: synthesis, structure and mechanical properties of amorphous coordination polymers, *Chem. Commun.*, 2007, 2802–2804.
18 S. Saha, B. Pal, K. S. Das, P. K. Ghose, A. Ghosh, A. De, A. K. Das, P. P. Ray and R. Mondal, Design of Dual Purpose Fe–metallogel for Magnetic Refrigeration and Fabrication of Schottky Barrier Diod, *ChemistrySelect*, 2022, **7**, e202203307.
19 S. Akhtar, S. Bala, A. De, K. S. Das, A. Adhikary, S. Jyotsna, P. Poddar and R. Mondal, Designing Multifunctional MOFs Using the Inorganic Motif [Cu3(μ3-OH)(μ-Pyz)] as an SBU and Their Properties, *Cryst. Growth Des.*, 2019, **19**, 992–1004.
20 B. Mondal, D. Bairagi, N. Nandi, B. Hansda, K. S. Das, C. J. C. Edwards-Gayle, V. Castelletto, I. W. Hamley and A. Banerjee, Peptide-Based Gel in Environmental Remediation:

Removal of Toxic Organic Dyes and Hazardous Pb^{2+} and Cd^{2+} Ions from Wastewater and Oil Spill Recovery, *Langmuir*, 2020, **36**, 12942–12953.

21 S. Akhtar, P. Singha, A. De, K. S. Das, S. Saha, S. Bala and R. Mondal, Construction of a series of metal-directed MOFs to explore their physical and chemical properties, *New J. Chem.*, 2021, **45**, 6438–6449.

22 C. Soman, A. Sebastian, M. K. Mahato, U. V. Varadarajub and E. Prasad, Multi-stimuli responsive and intrinsically luminescent polymer metallogel through ring opening copolymerization coupled with thiol-ene click chemistry, *Mater. Adv.*, 2022, **3**, 5458–5467.

23 X.-Q. Wang, W. Wang, G.-Q. Yin, Y.-X. Wang, C.-W. Zhang, J.-M. Shi, Y. Yu and H.-B. Yang, Cross-linked supramolecular polymer metallogels constructed *via* a self-sorting strategy and their multiple stimulus-response behaviors, *Chem. Commun.*, 2015, **51**, 16813–16816.

24 S. Majumdar, D. Mukherjee, G. Lepcha, K. K. Saha, K. S. Das, I. Pal, N. C. Mandal and B. Dey, Itaconic and citraconic acid directed thixotropic and self-healable supramolecular metallogels of M(II) (M = Co, Cu, Zn, and Cd) for the growth-inhibitory potency against human pathogenic microbes, *New J. Chem.*, 2023, **47**, 9643–9653.

25 X.-J. Sun, X. Zhang, H. Dong, D.-D. Yang, H.-L. Tang, Y.-C. Zhai, J.-Z. Wei and F.-M. Zhang, Porous metal–organic gel assisted by L-tartaricacid ligand for efficient and controllable drug delivery, *New J. Chem.*, 2018, **42**, 14789–14795.

26 A. Adhikary, K. S. Das, S. Saha, M. Roy and R. Mondal, A free-standing, self-healing multi-stimuli responsive gel showing cryogenic magnetic cooling, *Dalton Trans.*, 2020, **49**, 13487–13495.

27 K. S. Das, B. Pal, S. Saha, S. Akhtar, A. De, P. P. Ray and R. Mondal, Utilization of counter anions for charge transportation in the electrical device fabrication of Zn(II) metal–organic frameworks, *Dalton Trans.*, 2020, **49**, 17005–17016.

28 R. A. Kharod, J. L. Andrews and M. Dincă, Teaching Metal–Organic Frameworks to Conduct: Ion and Electron Transport in Metal–Organic Frameworks, *Annu. Rev. Mater. Res.*, 2022, **52**, 103.

29 S. Majumdar, B. Pal, G. Lepcha, K. S. Das, I. Pal, P. P. Ray and B. Dey, Establishment of different aliphatic amines-based rapid self-healing $Mg(OH)_2$ metallogels: exploring the morphology, rheology and intriguing semiconducting Schottky diode characteristics, *New J. Chem.*, 2023, **47**, 4752–4760.

30 G. Lepcha, T. Singha, S. Majumdar, A. K. Pradhan, K. S. Das, P. K. Datta and B. Dey, A semiconducting supramolecular novel Ni(II)–metallogel derived from 5-aminoisophthalic acid low molecular weight gelator: an efficient Schottky barrier diode application, *Dalton Trans.*, 2022, **51**, 13435–13443.

31 A. Jain, K. V. Rao, C. Kulkarni, A. George and S. J. George, Fluorescent coronene monoimide gels *via* H-bonding induced frustrated dipolar assembly, *Chem. Commun.*, 2012, **48**, 1467–1469.

32 H.-H. Yang, P.-P. Liu, J.-P. Hu, H. Fang, Q. Lin, Y. Hong, Y.-M. Zhang, W.-J. Qu and T.-B. Wei, A fluorescent supramolecular gel and its application in the ultrasensitive detection of CN by anion–π interactions, *Soft Matter*, 2020, **16**, 9876–9881.

33 D. Kim, M. Kang, H. Ha, C. S. Hong and M. Kim, Multiple functional groups in metal–organic frameworks and their positional regioisomerism, *Coord. Chem. Rev.*, 2021, **438**, 213892.

34 P. V. Dau, K. K. Tanabe and S. M. Cohen, Functional group effects on metal–organic framework topology, *Chem. Commun.*, 2012, **48**, 9370–9372.

35 S. Kim, B. Joarder, J. A. Hurd, J. Zhang, K. W. Dawson, B. S. Gelfand, N. E. Wong and G. K. H. Shimizu, Achieving Superprotonic Conduction in Metal−Organic Frameworks through Iterative Design Advances, *J. Am. Chem. Soc.*, 2018, **140**, 1077–1082.

36 D. W. Kang, K. S. Lim, K. J. Lee, J. H. Lee, W. R. Lee, J. H. Song, K. H. Yeom, J. Y. Kim and C. S. Hong, Cost-Effective, High-Performance Porous-Organic-Polymer Conductors Functionalized with Sulfonic Acid Groups by Direct Postsynthetic Substitution, *Angew. Chem., Int. Ed.*, 2016, **55**, 16123–16126.

37 H. Wu, F. Yang, X.-L. Lv, B. Wang, Y.-Z. Zhang, M.-J. Zhao and J.-R. Li, A stable porphyrinic metal–organic framework pore-functionalized by high-density carboxylic groups for proton conduction, *J. Mater. Chem. A*, 2017, **5**, 14525–14529.

38 P.-P. Chen, P. Ma, X. He, D. Svatunek, F. Liu and K. N. Houk, Computational Exploration of Ambiphilic Reactivity of Azides and Sustmann's Paradigmatic Parabola, *J. Org. Chem.*, 2021, **86**, 5792–5804.

39 S. Mukherjee, S. Ganguly, A. Chakraborty, A. Mandal and D. Das, Green Synthesis of Self Assembled Nanospherical Dysprosium MOFs: Selective and Efficient Detection of Picric Acid in Aqueous and Gas Phase, *ACS Sustainable Chem. Eng.*, 2019, **7**, 819–830.

40 X. Yan, T. R. Cook, J. B. Pollock, P. Wei, Y. Zhang, Y. Yu, F. Huang and P. J. Stang, Responsive Supramolecular Polymer Metallogel Constructed by Orthogonal Coordination-Driven Self-Assembly and Host/Guest Interactions, *J. Am. Chem. Soc.*, 2014, **136**, 4460–4463.

41 X.-Q. Wang, W. Wang, G.-Q. Yin, Y.-X. Wang, C.-W. Zhang, J.-M. Shi, Y. Yu and H.-B. Yang, Cross-linked supramolecular polymer metallogels constructed *via* a self-sorting strategy and their multiple stimulus-response behaviors, *Chem. Commun.*, 2015, **51**, 16813–16816.

42 S. Ganguly, P. Pachfule, S. Bala, A. Goswami, S. Bhattacharya and R. Mondal, Azide-Functionalized Lanthanide-Based Metal−Organic Frameworks Showing Selective CO_2 Gas Adsorption and Postsynthetic Cavity Expansion, *Inorg. Chem.*, 2013, **52**, 3588–3590.

43 A. Dey, S. Middya, R. Jana, M. Das, J. Datta, A. Layek and P. P. Ray, Light induced charge transport property analysis of nanostructured ZnS based Schottky diode, *J. Mater. Sci.: Mater. Electron.*, 2016, **27**, 6325–6335.

44 S. Sengupta and R. Mondal, Elusive Nanoscale Metal–Organic-Particle-Supported Metallogel Formation Using a Nonconventional Chelating Pyridine–Pyrazole-Based Bis-Amide Ligand, *Chem. – Eur. J.*, 2013, **19**, 5537–5541.

45 T. D. Hamilton, D.-K. Bučar, J. Baltrusaitis, D. R. Flanagan, Y. Li, S. Ghorai, A. V. Tivanski and L. R. MacGillivray, Thixotropic Hydrogel Derived from a Product of an Organic Solid-State Synthesis: Properties and Densities of Metal–Organic Nanoparticles, *J. Am. Chem. Soc.*, 2011, **133**, 3365–3371.

46 T. Bhattacharyya, R. Chaudhuri, K. S. Das, R. Mondal, S. Mandal and J. Dash, Cytidine-Derived Hydrogels with Tunable Antibacterial Activities, *ACS Appl. Bio Mater.*, 2019, **2**, 3171–3177.

47 C. Mahendar, Y. Kumar, M. K. Dixit and M. Dubey, An Li^{+}-enriched Co^{2+}-induced metallogel: a study on thixotropic rheological behaviour and conductance, *Soft Matter*, 2020, **16**, 3436–3442.

48 S. Majumdar, B. Pal, R. Sahu, K. S. Das, P. P. Ray and B. Dey, A croconate-directed supramolecular self-healable Cd(II)–metallogel with dispersed 2D-nanosheets of hexagonal boron nitride: a comparative outcome of the charge-transport phenomena and nonlinear rectifying behaviour of semiconducting diodes, *Dalton Trans.*, 2022, **51**, 9007–9016.

49 A. Dey, S. Middya, R. Jana, M. Das, J. Datta, A. Layek and P. P. Ray, Light induced charge transport property analysis of nanostructured ZnS based Schottky diode, *J. Mater. Sci.: Mater. Electron.*, 2016, **27**, 6325–6335.

50 E. H. Rhoderick, *Metal–Semiconductor Contacts*, Oxford University, Press, London, 1978.

51 S. K. Cheung and N. W. Cheung, Extraction of Schottky diode parameters from forward current-voltage characteristics, *Appl. Phys. Lett.*, 1986, **49**, 85–87.

52 A. Dey, A. Layek, A. Roychowdhury, M. Das, J. Datta, S. Middya, D. Das and P. P. Ray, Investigation of charge transport properties in less defective nanostructured ZnO based Schottky diode, *RSC Adv.*, 2015, **5**, 36560–36567.

53 R. K. Gupta and F. Yakuphanoglu, Photoconductive Schottky diode based on Al/p-Si/SnS_2/Ag for optical sensor applications, *Sol. Energy*, 2012, **86**, 1539–1545.

54 X. Miao, S. Tongay, M. K. Petterson, K. Berke, A. G. Rinzler, B. R. Appleton and A. F. Hebard, High Efficiency Graphene Solar Cells by Chemical Doping, *Nano Lett.*, 2012, **12**, 2745–2750.

55 P. W. M. Blom, M. J. M. de Jong and M. G. van Munster, Electric-field and temperature dependence of the hole mobility in poly(*p*-phenylene vinylene), *Phys. Rev. B: Condens. Matter Mater. Phys.*, 1997, **55**, R656–R659.

56 S. Sil, A. Dey, J. Dattaa, M. Das, R. Jana, S. Halder, J. Dhar, D. Sanyal and P. P. Ray, Analysis of interfaces in Bornite (Cu_5FeS_4) fabricated Schottky diode using impedance spectroscopy method and its photosensitive behaviour, *Mater. Res. Bull.*, 2018, **106**, 337.

57 S. Saha, K. S. Das, P. Pal, S. Hazra, A. Ghosh, S. Bala, A. Ghosh, A. K. Das and R. Mondal, A Silver-Based Integrated System Showing Mutually Inclusive Super Protonic Conductivity and Photoswitching Behavior, *Inorg. Chem.*, 2023, **62**, 3485–3497.

58 O. Basu, S. Mukhopadhyay, S. Laha and S. K. Das, Defect Engineering in a Metal–Organic Framework System to Achieve Super-Protonic Conductivity, *Chem. Mater.*, 2022, **34**, 6734–6743.

59 R. Moi, A. Ghorai, S. Banerjee and K. Biradha, Amino- and Sulfonate-Functionalized Metal–Organic Framework for Fabrication of Proton Exchange Membranes with Improved Proton Conductivity, *Cryst. Growth Des.*, 2020, **20**, 5557–5563.

60 R. Marschall, J. Rathouský and M. Wark, Ordered Functionalized Silica Materials with High Proton Conductivity, *Chem. Mater.*, 2007, **19**, 6401–6407.

61 S. Saha, M. Das, K. S. Das, R. Datta, S. Bala, J.-L. Liu, P. P. Ray and R. Mondal, Magnetic and Electric Properties of Pyrazole-Based Metal–Organic Frameworks Grafted With a Sulfonic Moiety, *Cryst. Growth Des.*, 2023, **23**, 1104–1118.

62 D. Zhang, G. Li, Y. Peng and L. Li, Synthesis of a Ternary Thiostannate with 3D Channel Decorated by Hydronium for High Proton Conductivity, *Inorg. Chem.*, 2017, **56**, 208–212.

63 S. Sarkar, S. Dutta, S. Chakrabarti, P. Bairi and T. Pal, Redox-Switchable Copper(I) Metallogel: A Metal–Organic Material for Selective and Naked-Eye Sensing of Picric Acid, *ACS Appl. Mater. Interfaces*, 2014, **6**, 6308–6316.

64 J. H. Jung, J. H. Lee, J. R. Silverman and G. John, Coordination polymer gels with important environmental and biological applications, *Chem. Soc. Rev.*, 2013, **42**, 924–936.